Supplementary Information

Online reprogramming electronic bits for *N* dimension fractal soft deformable structures

Fengjiao Bin,[1a] Jiaxu Meng, [1a] Wei Chen,[b,c] Ruishen Lou,[a] Xu Li,[a] Jiangman Sun,[d] Shikai Jing, [*a] Dengbao Xiao [*a]

a. Beijing Institute of Technology, Beijing 100021, P.R. China,

b. Beijing University of Technology, Beijing 100124, P.R. China

c. Beijing Aire Intech Eye Hospital, Beijing 100041, P.R. China

d.Beijing University of Chemical Technology, Beijing 100029, P.R. China

Table of content

[1] *Fengjiao Bin and Jiaxu Meng contributed equally to this work.*
E-mail: Jingshikai@bit.edu.cn, xdbhangtian@163.com

1. Materials preparation and dynamic mechanical analysis

1.1 Materials preparation

The soft structure was fabricated through the solution polymerization technique, with the required chemicals detailed in Table 1. The base material, consisting of shape-memory polymers (SMPs), was formulated by blending aliphatic polyurethane diacrylate, 2-phenoxyethyl acrylate, isobornyl acrylate, and azobisisobutyronitrile. NdFeB power, used as a filler, was mixed with a specific amount of pyrogenic silica during the solution blending to enhance its suspension. This addition aimed to improve the homogeneity of the mixture between the base material and the filler, ensuring a uniform distribution throughout the structure.

Supplementary Table 1 Materials required for the experiment.

Name	Mass (g)
Aliphatic polyurethane diacrylate (Resinous)	5.0
2-Phenoxyethyl acrylate (Liquid)	15.0
Isobornyl acrylate (Liquid)	30.0
Azobisisobutyronitrile (Powdered)	0.2
Fumed silica (0.2μm, Powdered)	1.0
NdFeB powder (5μm, Powdered)	67.8

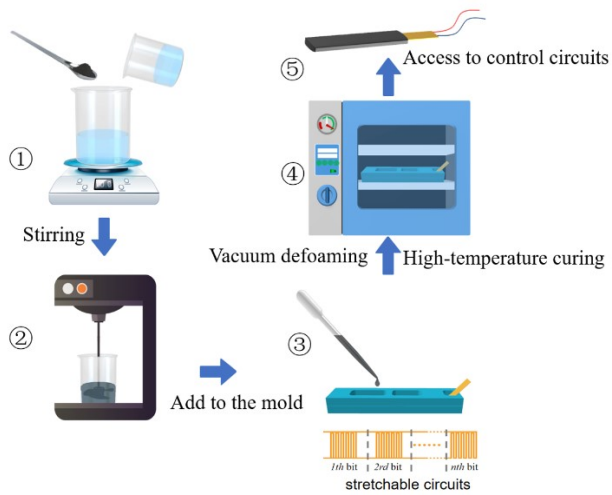

Supplementary Fig. 1 Preparation process for online reprogramming electronic bits.

The procedure of preparing the SMPs solution is outlined in Fig. 1, as detailed below:

Fundamental materials were listed in Table 1 according to experimental protocols. Care should be taken when adding pyrogenic silica to prevent it from dispersing into the air. NdFeB powder is flammable and flames or static electricity should be avoided during handling. Given that NdFeB powder is prone to oxidation, any remaining powder should be sealed and stored immediately after weighing.

Begin by uniformly mixing the chemicals listed in Table 1 through stirring. Utilize a shear mixer to ensure thorough dispersion of the pyrogenic silica, thereby enhancing the suspension of the NdFeB powder in the solution. The stirring speed should be set to 1400 to 1800 rpm, with the process continuing for 40 to 50 minutes to prepare the SMPs solution. Next, debubble the solution by placing it in a vacuum oven. Afterward, install the heating wire at the center of the mold, and sequentially introduce the solution into the mold in four stages using a dropper. Place the mold in an oven for heat curing. Turn on the heating switch, and when the oven temperature reaches 80 degrees Celsius, maintain this temperature for 4 hours. Then, increase the temperature to 120 degrees Celsius and hold it for half an hour.

1.2 Dynamic mechanical analysis (DMA)

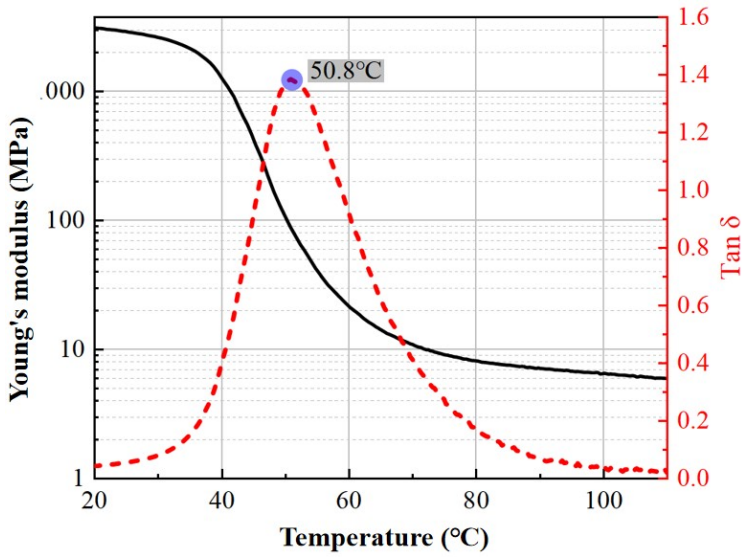

Supplementary Fig. 2: DMA data.

The prepared material specimens was measured Young's modulus, glass transition temperature and the damping coefficient tanδ by DMA. The DMA instrument used was the

DMA8000 model from PE made in USA, with sample dimensions of 20mm×20mm×2mm. The heating rate was set at 3°C/min, covering a temperature range from 20°C to 120°C at a frequency of 1Hz. Experimental data were showed in Fig. 2 and indicateed a sharp decrease in Young's modulus as the temperature increases to 50.8°C, with values approaching a constant level below 40°C and above 70°C. This step-like state is apt for describing distinctly different states, akin to the binary state transitions presented in Fig. 2b of the manuscript.

2. Theoretical analysis

Theoretical analysis is conducted based on the deformation of a typical two-element deformable structure. The force behavior of the flexible structure under a uniform magnetic field is illustrated in **Supplementary Fig. 3**. In the figure, ***B*** represents the magnetic field strength, ***M*** is the bending moment, φ denotes the magnetic field angle, θ_a indicates the beam end rotation angle, l represents the length of the bits, and E, A, and I are sectional parameters of the bits.

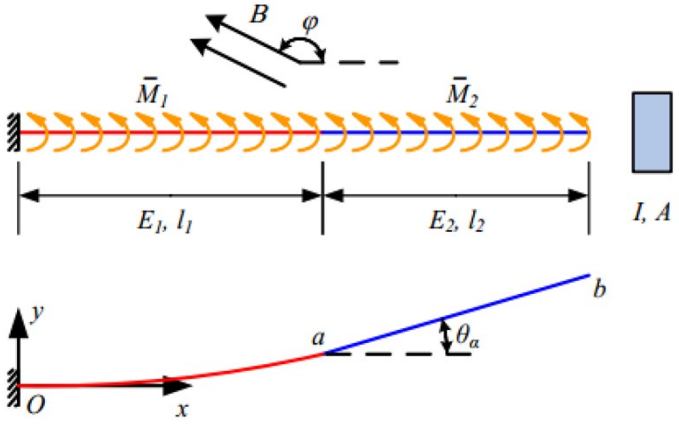

Supplementary Fig. 3 Forces acting on a soft structure in a uniform magnetic field.

The right bit can be considered a rigid body, subject only to rigid displacement and rotation due to the deformation of the left bit. In a uniform magnetic field, the deformation of the left bit is determined by combining the deformation caused by its own uniformly distributed bending moment with that resulting from the concentrated bending moment applied by the right bit. The deformation of the left bit, resulting from a uniformly distributed bending moment, is governed by the following equilibrium equation.

Based on Wang' s work[1], the rotation angle θ_L of the left end can be calculated as follows:

$$\frac{EId^2\theta}{A\,ds^2}+\frac{\partial}{\partial\theta}(RM\cdot B)=0 \quad . \tag{S1}$$

$$L_1^2=\frac{E_1 I}{2|\overline{M}||\overline{B}|A}\Phi^2(\varphi,\theta_L) \tag{S2}$$

$$\begin{aligned}\theta_L &= \int_0^{\theta_L}\left(\cos(\varphi-\theta_L)-\cos(\varphi-\theta)\right)^{-1/2}d\theta \\ &= \frac{2}{\sqrt{\cos(\varphi-\theta_L)-1}}\left[F\left(\frac{\varphi-\theta_L}{2},\csc\left(\frac{\varphi-\theta_L}{2}\right)\right)-F\left(\frac{\varphi}{2},\csc\left(\frac{\varphi-\theta_L}{2}\right)\right)\right]\end{aligned} \tag{S3}$$

$$F(\phi,k)=\int_0^{\phi}\frac{d\theta}{\sqrt{1-k^2\sin^2\theta}} \quad . \tag{S4}$$

The concentrated bending moment generated in the right section of the beam can be determined from the angle at the left end. The concentrated bending moment applied to the right section of the beam is calculated using the theory of small deformations[1] and then superimposed onto the left section to ascertain the beam's total deformation. The forces acting on any section of the curved beam are depicted in **Supplementary Fig. 4.**

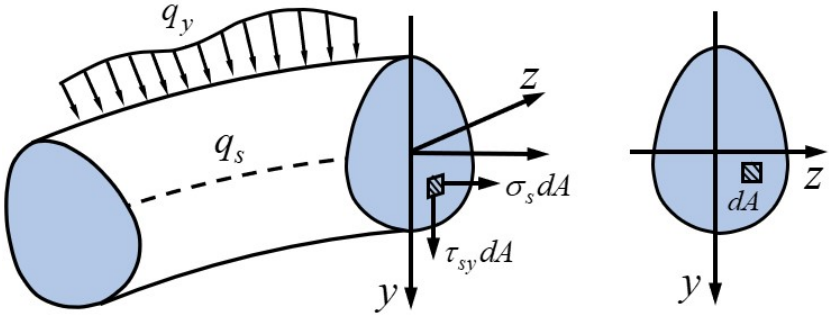

Supplementary Fig. 4 Forces acting on section of a bent bit.

The differential equation describing its deflection curve is given by:

$$\begin{cases} \frac{du}{ds} - \frac{v}{R} = \frac{N}{EA} - \frac{M}{EAR} \\ \frac{d^2v}{ds^2} + \frac{v}{R^2} = -\frac{M}{EJ_z} \end{cases}, \tag{S5}$$

where u and v represent the tangential and normal displacements of the cross-section's centroid along the curved beam axis s, R is the radius of curvature at the cross-section, and N and M are the axial force and bending moment at the cross-section, respectively. J_Z is the moment generated by considering varying fiber lengths across different locations of the curved beam's cross-section, with its calculation formula presented as follows:

$$J_z = \int_A \frac{y^2 dA}{(1 - \frac{y}{R})}. \tag{S6}$$

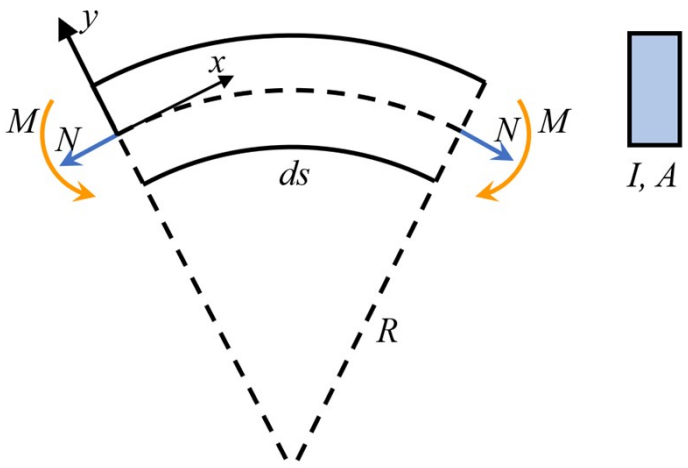

Supplementary Fig. 5 Distribution of forces in a curved beam.

For a curved beam with a rectangular cross-section:

$$J_z = R^3 b \ln \frac{2R + h}{2R - h} - R^2 bh. \tag{S7}$$

Considering that the concentrated bending moment M varies with the rotation angle at the left end of the beam, the overall deformation of the curved beam is solved through an iterative process, described as follows:

(1) Assume the magnetic induction intensity at the *i*-th iteration step is B_i and the rotation angle of the left beam end is θ_{ai}, where $\theta_{a1}=\theta_L$. Consequently, the bending moment M_{ai} at the beam end for the current iteration is defined by

$$M_{ai} = AL_2|\overline{M}||\overline{B_i}|\sin(\varphi - \theta_{ai}) \quad . \tag{S8}$$

(2) In the scenario presently examined, the integration of Equation (S8) into Equation (S5) yields the following derived outcome:

$$\begin{cases} \dfrac{du}{ds} - \dfrac{v}{R} = -\dfrac{M_{ai}}{E_1 AR} \\ \dfrac{d^2v}{ds^2} + \dfrac{v}{R^2} = -\dfrac{M_{ai}}{E_1 J_z} \end{cases} . \tag{S9}$$

The radius of curvature for the curved beam as defined in Equation (S9) is defined by

$$R^2 = \left(\frac{d\theta}{ds}\right)^{-2} . \tag{S10}$$

Equation (S9) is a system of second-order linear ordinary differential equations with non-constant coefficients. Since R varies as a function of s, an explicit solution to this system is not feasible. As a result, numerical methods are employed for its resolution. The geometric configuration of the curved beam on the left side is described below[1]:

$$\begin{cases} \dfrac{d\theta}{ds} = \sqrt{\dfrac{2|\overline{M}||\overline{B}|A}{E_1 I}}\sqrt{\cos(\varphi - \theta_L) - \cos(\varphi - \theta)} \\ \dfrac{dx}{ds} = \cos(\theta) \\ \dfrac{dy}{ds} = \sin(\theta) \end{cases} . \tag{S11}$$

Integrating Equation (S9) and (S11) allows for the calculation of the values for x, y, θ, u and v. According to the principle of superposition in solid mechanics[2], the deflection curve of the curved beam is determined as follows:

$$\begin{cases} x' = x + \cos(\theta)u + \sin(\theta)v \\ y' = y - \cos(\theta)v + \sin(\theta)u \end{cases} . \tag{S12}$$

At this stage, the angle at the end of the beam is defined as:

$$\theta_{ai+1} = arctan\left(\frac{dy'}{dx'}|_{s=L_1}\right). \quad \text{(S13)}$$

(1) The iteration continues until B_i=B, at which junction the coordinates at the beam's end, denoted as (x_a, y_a), correspond to the rotation angle, noted as θ_a.

By incorporating Equation (S8), we conclude that the beam on the right side is rigid, with the position of its free end determined by:

$$\begin{cases} x_b = x_a + L_2\cos(\theta_a) = x_a + M_{ai}\cos(\theta_a)/A|\overline{M}||\overline{B_i}|\sin(\varphi - \theta_{ai}) \\ y_b = y_a + L_2\sin(\theta_a) = y_a + M_{ai}\sin(\theta_a)/A|\overline{M}||\overline{B_i}|\sin(\varphi - \theta_{ai}) \end{cases}. \quad \text{(S24)}$$

As mentioned earlier, the deformation capability of the soft structure is determined by several factors including the strength and direction of the magnetic field, the unit bending resistance cross-section factor, the number of units, and the magnetic strength of each unit.

3. Numerical simulation

The simulation process is detailed as follows:

(1) The air domain simulates the external environment surrounding the soft structure, while a fixed clamp represents the clamping state. Fixed constraints are applied to the upper and lower plates and the end of the soft structure, with the remainder left free.

(2) The simulation model is solved using the 'magnetic field', 'no current' and 'solid mechanics' physical fields. For the magnetic field analysis, a one-dimensional uniform magnetic field of 280mT is introduced into the air domain in the direction indicated in Supplementary Fig. 5. In simulating mechanical deformation, the effect of temperature on the material's Young's modulus is simplified through interpolating of the temperature-dependence curve measured by the Dynamic Mechanical Analysis (DMA) experiments.

(3) To simulate the bending deformation driven by magnetic field forces on the magnetic particles, the mechanics and magnetic fields are coupled in COMSOL to compute the magnetic field force applied to the soft structure. Subsequently, a boundary load module is introduced within the solid mechanics field to apply the calculated magnetic field force.

(4) Mesh size is tailored to the computational demands of different regions. The area within reach of bending is refined to improve the accuracy of the results, whereas regions distant

from the soft structure employ a coarser mesh to reduce computational time. Given that the model involves large deformation finite element simulation, a dynamic mesh is implemented. This mesh adapts during bending, being redefined to yield more precise simulation outcomes.

4. Experiments

4.1. The experiment setup

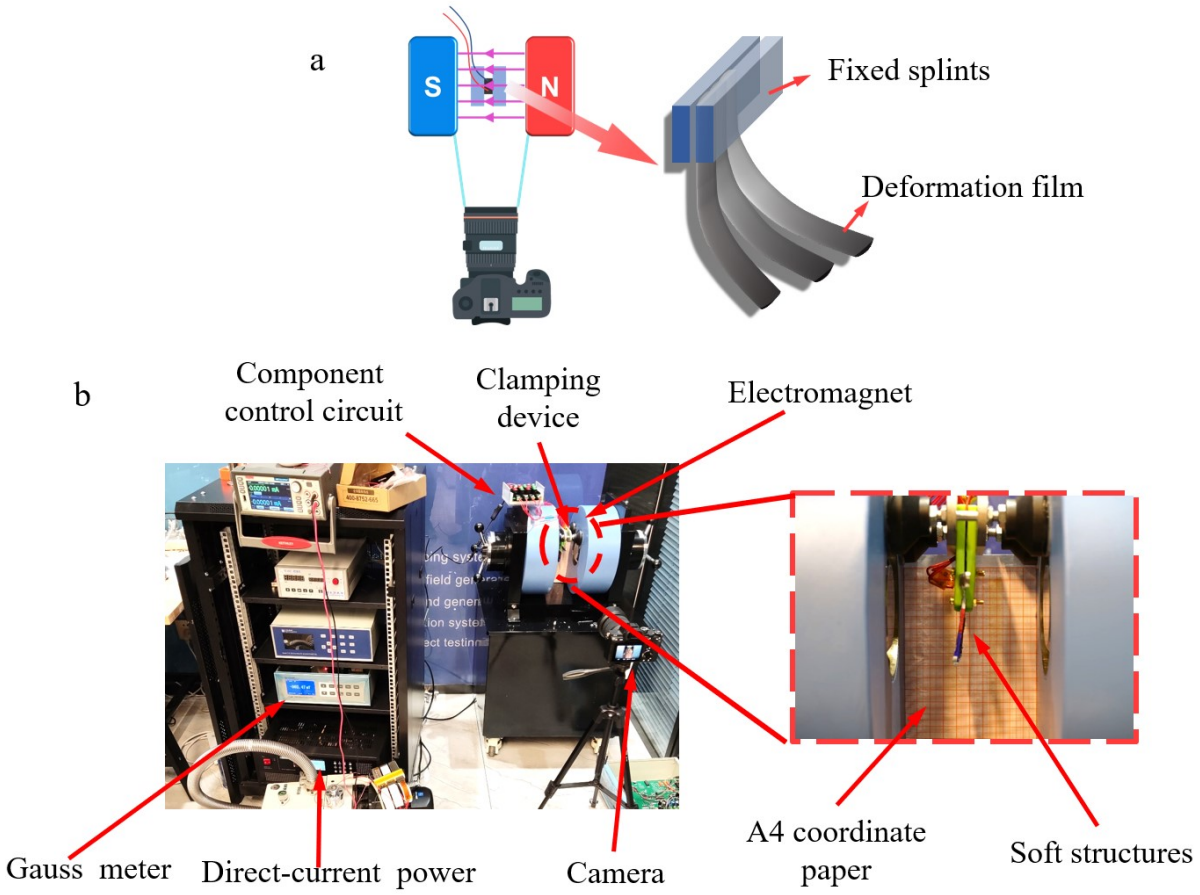

Supplementary Fig. 6 Experimental setup: a) schematic diagram, b) magnetic field generator and data acquisition equipment.

The magnetic field generator, as depicted in supplementary Fig. 6, consists of an electromagnet, an electromagnet power supply, a Gauss meter, a test stand, and a sample clamping device. The electromagnet generates a one-dimensional uniform magnetic field，with its intensity regulated by modifying the input current. Furthermore, the direction of the magnetic field's poles can be controlled by reversing the current's direction. In this experiment,

the electromagnet can produce a maximum magnetic field of 3500 Gauss. The electromagnet power supply uses an F2030 high-precision digital power source to deliver a stable current to the electromagnet. The output range of the power supply spans from -10 to 10A, featuring high step resolution accuracy of ±0.2% for 1mA and 5mA outputs, and ±0.1% for 10 outputs. The Gauss meter, model CH-1300, offers a measurement range of ±3T, a resolution of 0.1mT, and an accuracy of ±0.50%. The measurement accuracy of these instruments is sufficient to meet the research requirements of this project.

4.2. Online reprogramming soft strip structure

The process of changing the magnetic field and controlling temperature to switch binary states via the bit's stretchable heater circuit, resulting in sine and cosine curve deformations, is illustrated in Supplementary Fig. 7. The main steps are outlined as follows:

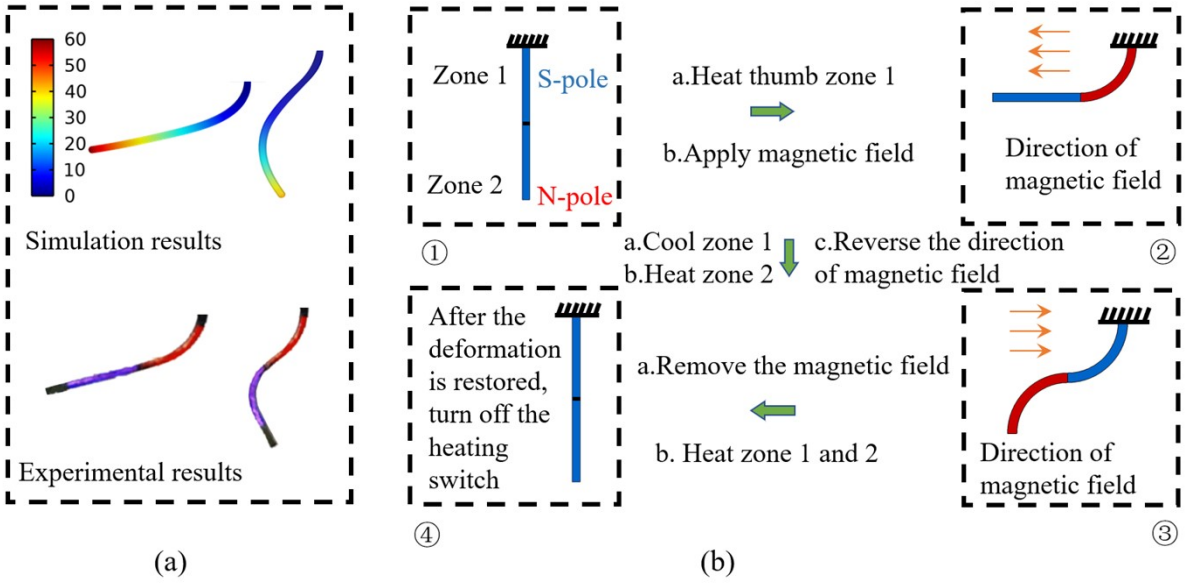

Supplementary Fig. 7 Online reprogramming of thermal controls and applied magnetic field to two bits during sinusoidal deformation of a soft structure.

(1) Turn on the heating switch zone 1 of the soft structure and heat it to above 90℃, which takes approximately one minute. Following this, apply and maintain a uniform magnetic field until the magnetic flux density increases to 3000 Gauss.

(2) Turn off the heating switch for zone 1 of the soft structure. Zone 1 starts cooling for approximately one and a half minutes, and the soft structure in zone 1 begins to solidify, preserving the previous deformation owing to the external magnetic field.

(3) Turn on the heating switch in zone 2 and heat it to above 90℃. Subsequently, reverse the direction of the magnetic field by changing the polarity of the input current to the electromagnet. Zone 2 rapidly bends in the opposite direction, whereas zone 1 performs minimal deformation due to its cooled state and large Young's modulus.

(4) Turn off the heating switch for zone 2 of the soft structure. Zone 2 cools to room temperature, taking about one and a half minutes, while zone 1 solidifies, preserving its previous deformation state due to the external magnetic field. At this point, the bending deformation of the soft structure exhibits a sine-cosine profile.

(5) Turn off the magnetic field and turn on the heating switches of both zones 1 and 2 until the soft structure reverts to its initial deformation state.

4.3. Online reprogramming hand-shaped soft structure

Soft structures, equipped with multiple independent bits, have the capacity to perform complex deformations. We have designed a hand-shaped structure, as depicted in supplementary Fig. 8a, where the palm, manufactured through 3D printing, supports five strip structures symbolizing the fingers.

Through the design of an experimental scheme, the hand-shaped structure successfully executed the "OK" gesture. This experimental setup is showed in supplementary Fig. 8, with the main steps detailed as follows:

(1) Turn on the heating switch for zone 1 in the thumb area and heat it to above 90℃. Following this, a 3000 Gauss uniform magnetic field is applied, causing rapid deformation of the thumb area due to magnetic field.

(2) Turn off the heating switch for zone 1 of the thumb, the thumb begins to solidify, preserving its previous deformation due to the external magnetic field’s influence.

(3) Turn on the heating switch for zone 1 of the index finger and increase its temperature to above 90℃. Change the direction of the magnetic field to 38° relative to the palm’s normal. This causes the index finger to bend due to the magnetic force, resulting in the hand-shaped structure forming an "OK" gesture, as shown in Supplementary Fig. 8c.

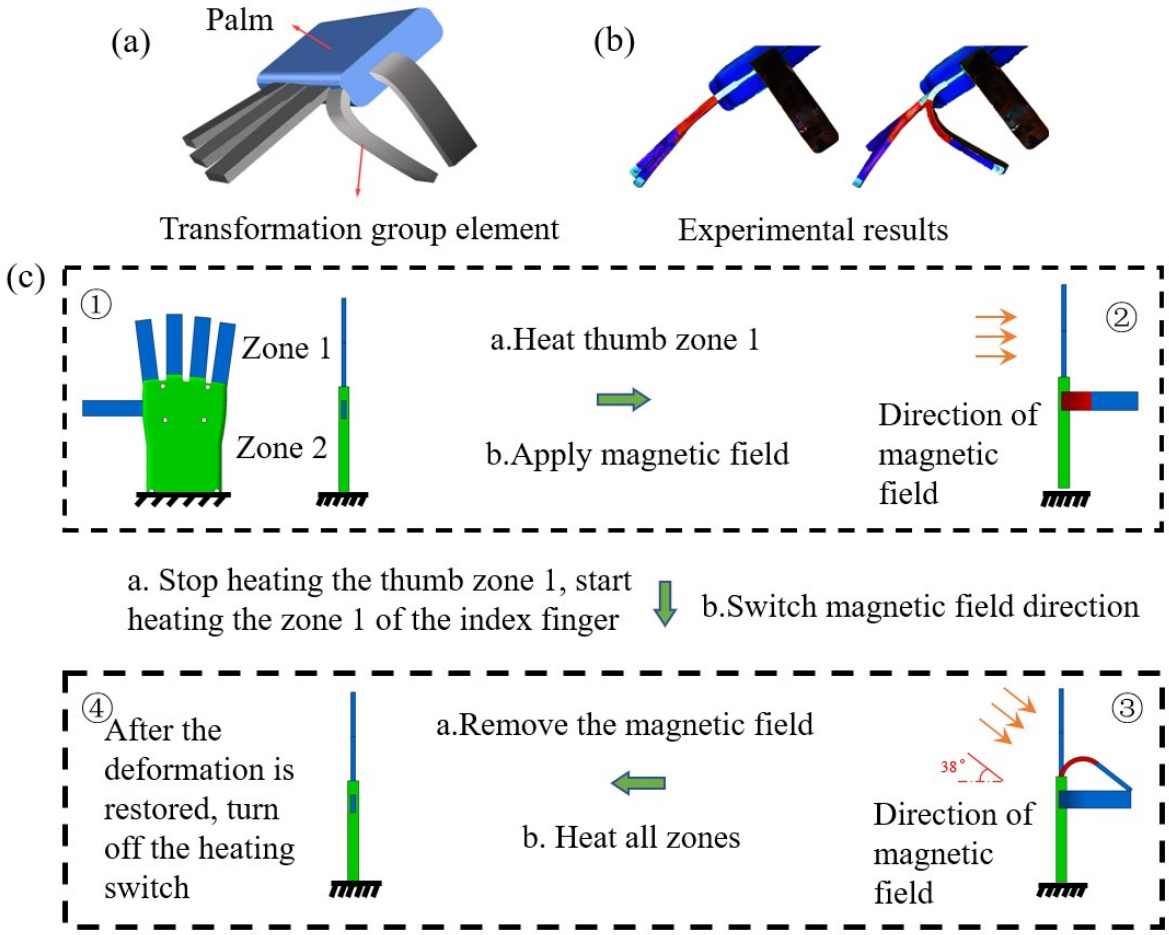

Supplementary Fig. 8 Reprogramming hand-shaped structure: a) demonstration of "OK"

4.4. Error analysis

The experimental deformation results in Figure 4 were compared with the simulation results, using the maximum displacement at the end of the flexible strip to calculate the error. The comparison between the experiment and the error is shown in Supplementary Fig. 9, and the related errors were provided in Supplementary Table 2, where it could be observed that the maximum displacement error at the end was less than 15%. The numbers of the flexible strips in the figure correspond to those in the table.

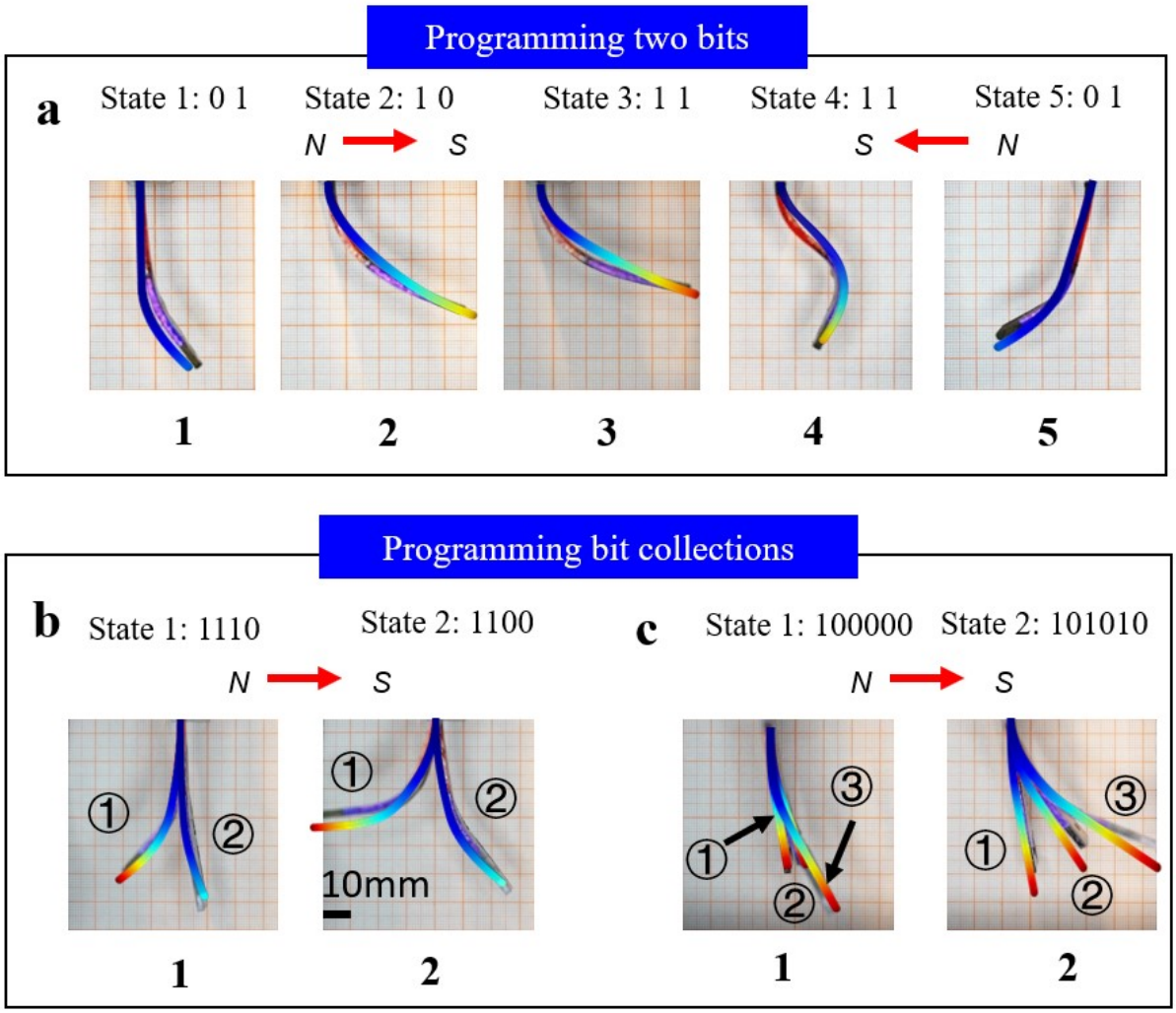

Supplementary Fig. 9 Comparison between simulation and experimental results

Supplementary Table 2 The relative error between experiment and simulation

No.		Simulation Displacement(mm)	Experimental Displacement(mm)	Related error@ (%)
a-1		26.23	27.86	5.85
a-2		51.47	48.88	5.30
a-3		54.71	52.48	4.25
a-4		7.67	8.60	10.81
a-5		22.25	24.17	7.94
b-1	□	28.43	26.25	8.30
	□	4.78	5.10	6.27

b-2	□	51.65	49.40	4.55
	□	24.12	25.30	4.66
c-1	□	3.01	3.16	4.75
	□	7.53	7.07	6.51
	□	21.55	19.92	8.18
c-2	□	8.35	7.28	14.70
	□	22.23	24.04	7.53
	□	53.56	56.08	4.49

@Relative error = (Simulation-Experiment)/ Experiment×100%

Experiment errors: Experimental errors are often caused by deviations in magnetic field application angle, where the actual magnetic field direction may differ from the theoretical setup, affecting the sample's response. Additionally, variations in equipment performance, such as magnetic field strength and uniformity, can further impact the accuracy of experimental data.

Simulation errors: Simulation errors typically arise from model simplifications, including insufficient mesh resolution and neglecting complex physical phenomena. Numerical approximations, such as instability and rounding errors during computations, also contribute to deviations from real-world results.

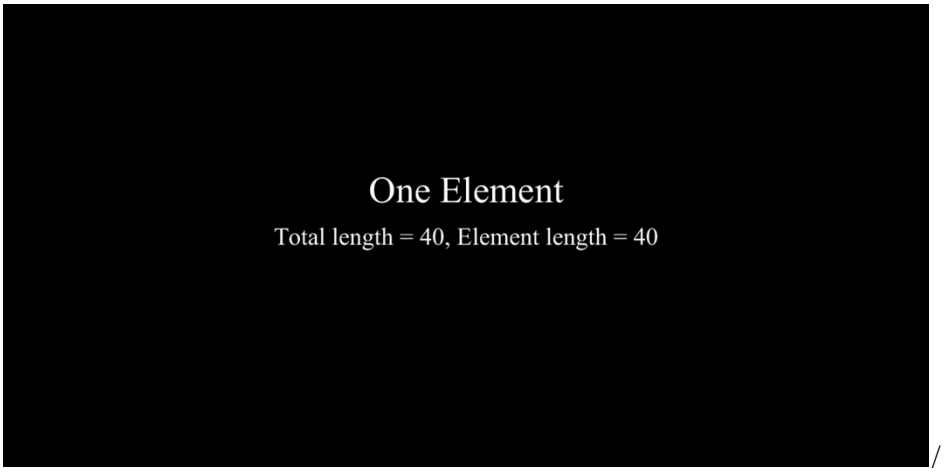

/

(a)

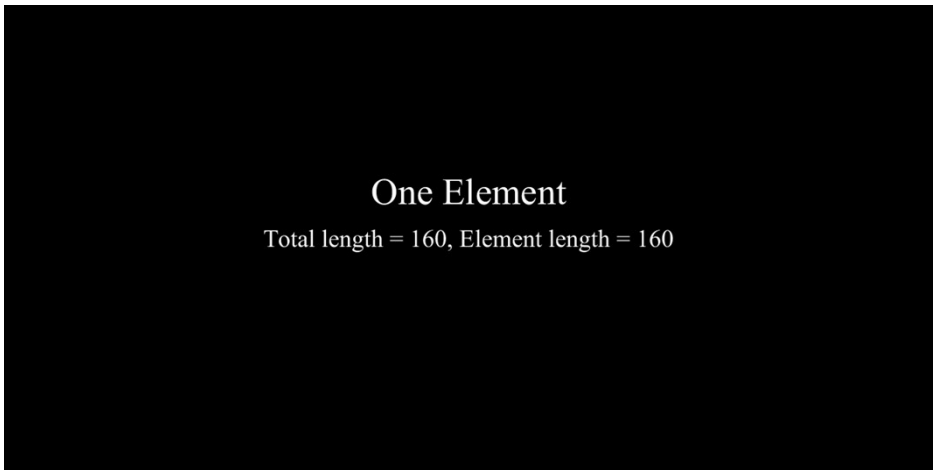

(b)

Supplementary Video 1 a) variation in deformation of soft structures with the number of bits, b) influence of bit size on soft structure deformation.

Video 1a reveals that with an increasing number n of bits, by adjusting the magnetic field $\boldsymbol{B}$ applied to the *i-th* bit, as indicated in the video's upper right corner, the soft structure obtains progressively complex deformations. The fractal dimension results, displayed in the lower right corner, change with the bit count, further evidencing the soft structure's capability for complex deformation morphologies. Likewise, by increasing the number of bits and continuously reducing the length of each newly added bit, the soft structure demonstrates an expanding range of programmable deformation morphologies in Video 1b.

1. L. Wang, Y. Kim, C. F. Guo and X. Zhao, *Journal of the Mechanics and Physics of Solids*, 2020, **142**, 104045.
2. S. Timoshenko, *New. York McGraw—Hil1*, 1970, **970**, 279-291.